Carbon 184 (2021) 492–503

Contents lists available at ScienceDirect

Carbon

journal homepage: www.elsevier.com/locate/carbon

Research Paper

Prediction and optimization of the thermal transport in hybrid carbon-boron nitride honeycombs using machine learning

Yao Du , Penghua Ying , Jin Zhang *

School of Science, Harbin Institute of Technology, Shenzhen, 518055, China

ARTICLE INFO

Article history:
Received 7 June 2021
Received in revised form
13 August 2021
Accepted 16 August 2021
Available online 19 August 2021

Keywords:
Carbon honeycombs
Boron nitride honeycombs
Machine learning
Molecular dynamic simulations
Thermal conductivity

ABSTRACT

The recently discovered carbon honeycombs (CHCs) and boron nitride honeycombs (BNHCs) are found to have the similar molecular structures but different thermal properties. Thus, through appropriately patching together CHCs and BNHCs, the hybrid carbon-boron nitride honeycombs (C–BNHCs) with tunable thermal conductivity can be achieved. In this paper, the machine learning (ML) method together with molecular dynamics simulations is employed to study the thermal transport property of C–BNHCs, and also utilized to design the structures of C–BNHCs for the specific thermal conductivity. Our forward learning study reveals a big difference in the thermal conductivities of C–BNHCs with the same BNHC doping level but different doping arrangements. Meanwhile, a nonmonotonic relation is observed between the thermal conductivity of C–BNHCs and their doping concentration, which, according to our analyses of the phonon density of states and spectral thermal conductivity, is attributed to the complicated phonon scattering behaviors in C–BNHCs. In addition, our ML-based method exhibits the high accuracy and efficiency in the inverse design of C–BNHCs with any specific thermal conductivity. Moreover, as for a target thermal conductivity, the present ML-based inverse design method can output numerous potential optimal structures at once for C–BNHCs, which will greatly shorten the design period of C–BNHCs.

1. Introduction

Inspired by the discoveries and synthesis of some new carbon and boron nitride materials at the nanoscale such as one-dimensional (1D) carbon nanotubes (CNTs) [1], 1D boron nitride nanotubes (BNNTs) [2], two-dimensional (2D) graphene [3] and 2D hexagonal boron nitride (hBN) [4,5], vast scientific efforts are currently devoted to study the physical properties of these new carbon and BN allotropes and, accordingly, investigate the potential engineering applications of these new materials. For instance, an ultrahigh Young's modulus of ~1 TPa and an extremely large thermal conductivity of ~6600 W/mK are observed in CNTs [6–8], which are widely used in nano-sensors and composite materials [9,10]. Similarly, graphene is reported to possess the extraordinary mechanical and thermal properties involving the Young's modulus of ~1 TPa, the tensile strength of 130 GPa [11] and a prominent thermal conductivity of ~4000 W/mK [12,13], which make graphene appealing in the applications of thermoelectric devices and nanocomposites [14–16]. As the analogues of CNTs, BNNTs are similarly found to possess a large axial Young's modulus of ~1.2 TPa [17] and a high thermal conductivity of ~400 W/mK [18]. Meanwhile, the BNNT uniquely is a wide band gap semiconductor with the distinguishable chemical stability [19,20], which thus can be treated as an important semiconducting and encapsulating material at the nanoscale [21,22]. The 2D hBN nanosheets have an ultrawide band gap [23], a high thermal conductivity [24–26] and a large Young's modulus [27,28], all of which are comparable to those of their 1D BNNT counterparts. Thus, hBN nanosheets are expected to serve as the important matrices for high-performance nanocomposites [29,30] and also the important building blocks for next-generation electronic devices [31].

Considering the fact that the low-dimensional carbon nanomaterials and their BN counterparts have the similarity in their atomic structures but have the difference in some material properties, researchers also have made a great deal of efforts to explore the synergy of the distinctive material properties by fabricating the hybrid C-BN nanomaterials. These C-BN nanomaterials are expected to possess the physical properties different from their pure components and thus have the broader engineering applications.

* Corresponding author.
E-mail address: jinzhang@hit.edu.cn (J. Zhang).

https://doi.org/10.1016/j.carbon.2021.08.035
0008-6223/

Recently, the hybrid graphene-hBN sheets have been successfully synthesized in experiments [32–34]. The physical performance of these heterostructures can be significantly modified by changing the doping concentration of their carbon or BN components. For examples, the piezoelectric coefficient of hybrid graphene-hBN sheet can be significantly increased by increasing the concentration of carbon component [35]. Meanwhile, the Young's modulus and thermal conductivity of hybrid graphene-hBN sheets and C-BN nanotubes are found to increase as the doping concentration of carbon component increases [36–39].

Although the aforementioned carbon and BN nanomaterials such as CNTs, BNNTs, graphene, hBN nanosheets and their heterostructures possess many remarkable properties, the low-dimensional structures of these materials greatly restrict their further engineering applications. Under this circumstance, fabricating new three-dimensional (3D) carbon and BN nanomaterials having properties almost comparable to their low-dimensional counterparts is receiving increasing attention from the material community. Recently, 3D carbon honeycombs (CHCs) comprised of graphene components have been synthesized successfully in experiments [40]. Many studies have revealed that CHCs possess numerous prominent properties involving the low density, large surface area per unit mass and high specific strength [40–45], which indicate that CHCs have great potential applications in gas and liquid storage and are suitable to serve as the composite matrices [40,46,47]. Similarly, the BN honeycomb (BNHC) has been theoretically confirmed as a new stable 3D BN nanomaterial [48–50], whose atomic configuration is analogous to that of its CHC counterpart. Compared with CHCs, BNHCs are reported to possess the unique piezopotential property [51,52]. In addition, both the mechanical and thermal transport properties of BNHCs are found to greatly lower than those of CHCs [52–54]. Inspired by the successful fabrication of 2D hybrid C-BN nanomaterials in experiments and the very different material properties observed between CHCs and BNHCs, it is expected to establish 3D hybrid C-BN honeycombs (C–BNHCs) comprised of both BNHC and CHC cells in the near future, which may have the wide tunable material properties between those of pure BNHCs and CHCs. Thus, optimizing the BNHC or CHC concentration in C–BNHCs and designing the pattern of C–BNHC structures play the crucial roles in the future material design of hybrid C–BNHCs.

In general, the conventional artificial design and automated design are two methods widely used to design the materials with required properties. It is noted that the artificial design often depends on heuristic hypothesis or intuitive methodologies derived from numerous errors and trials, which thus impede its application in material structure design and optimization. In order to overcome the limitation of artificial design methods, the emerging advanced computational algorithms such as machine learning (ML), topological optimization and generative algorithms have been recently proposed for designing material structures automatically. Especially, the ML-based methods have been widely utilized in designing the molecular structures of complex nanomaterials to satisfy some specific requirements. For examples, the ML method has been employed to design the kirigami-inspired graphene for searching optimal structures with the largest ultimate strain [55,56]. Meanwhile, the hole distribution in porous graphene has been optimized via ML to obtain target structures with desired thermal conductivity [57,58] and mechanical properties [59,60]. Motivated by aforementioned studies, it is of great interest to use the ML method to design the structures of C–BNHCs to make them possess some specific material properties such as the required thermal conductivity.

In this paper, through combing the ML method and classical molecular dynamics (MD) simulations, we investigate the thermal transport property of C–BNHCs and also propose an inverse design method for designing the structure of C–BNHCs with the required thermal conductivity. Here, the impacts of the concentration and arrangement of doping BNHC cells on the thermal conductivity of C–BNHCs are analyzed carefully with the help of a convolutional neural network (CNN), which is modified based on the VGGNet [61]. With the aid of the CNN, a ML-based inverse structural optimization method is developed for searching optimal structures possessing the required thermal conductivity among a large-scale design space. The obtained results indicate that the present ML-based method is able to find plenty optimal C–BNHC structures possessing the target thermal conductivity efficiently, accurately and practically.

2. Models and methodology

2.1. Workflow

In present work, the workflow illustrated in Fig. 1 was employed to investigate the thermal conductivity of a series of C–BNHCs constructed and, meanwhile, to design the structure of C–BNHCs with desired thermal transport property. In general, the workflow contains the following three steps. The first step is to construct numerous models and a large-scale data set as shown in Fig. 1(a). During this step, different atomic structures of C–BNHCs were generated by a random geometry generator. The thermal conductivities of them were computed by the nonequilibrium molecular dynamics (NEMD) simulations, which were denoted as the true thermal conductivities. Here, the grayscale images representing the top-views of C–BNHC structures and their thermal conductivities were assembled together to construct the sample library for the later ML-based method. The second step is to define and optimize the CNN model shown in Fig. 1(b). Based on the obtained CNN model, the influence of BNHC concentration on the thermal conductivity of C–BNHCs can be evaluated. The third step is to retrain the CNN model with a new sample library to seek structures of C–BNHCs with some required thermal conductivities [see in Fig. 1(c)]. Based on the retrained CNN model enhanced by an evolutionary approach during the iterations, we can design the C–BNHC structures with desired thermal transport properties efficiently. In what follows, some techniques employed in these three steps will be briefly described.

2.2. Model construction

The C–BNHC structures considered in the present study were constructed with the following procedures. Initially, as demonstrated in Fig. 2(a), the pure CHC structures were constructed, which were composed of the armchair-edged graphene nanoribbons with a length l of 7.38 Å [see in Fig. 2(c)]. Afterwards, some cells in CHCs were randomly changed into BNHC cells. Here, the selection of random replacements was determined by the random geometry generator as shown in Fig. 1(a), where “1” and “0” denote BNHC and CHC cells, respectively. In generating C–BNHC structures through this method, some cell walls (graphene nanoribbons) of CHC were replaced by armchair-edged BN nanoribbons with the same length. After this treatment, as shown Fig. 2(b), a series of C–BNHCs with different BNHC concentrations can be constructed. It is noted that in CHCs, every three adjacent graphene nanoribbons are linked together by a line of sp^3-bonded carbon atoms as shown in Fig. 2(c). However, due to the existence of some BN nanoribbon components in C–BNHCs, in addition to the triple junctions of graphene nanoribbons, some triple junctions comprised of one graphene nanoribbon and two BN nanoribbons are also observed [see in Fig. 2(d)].

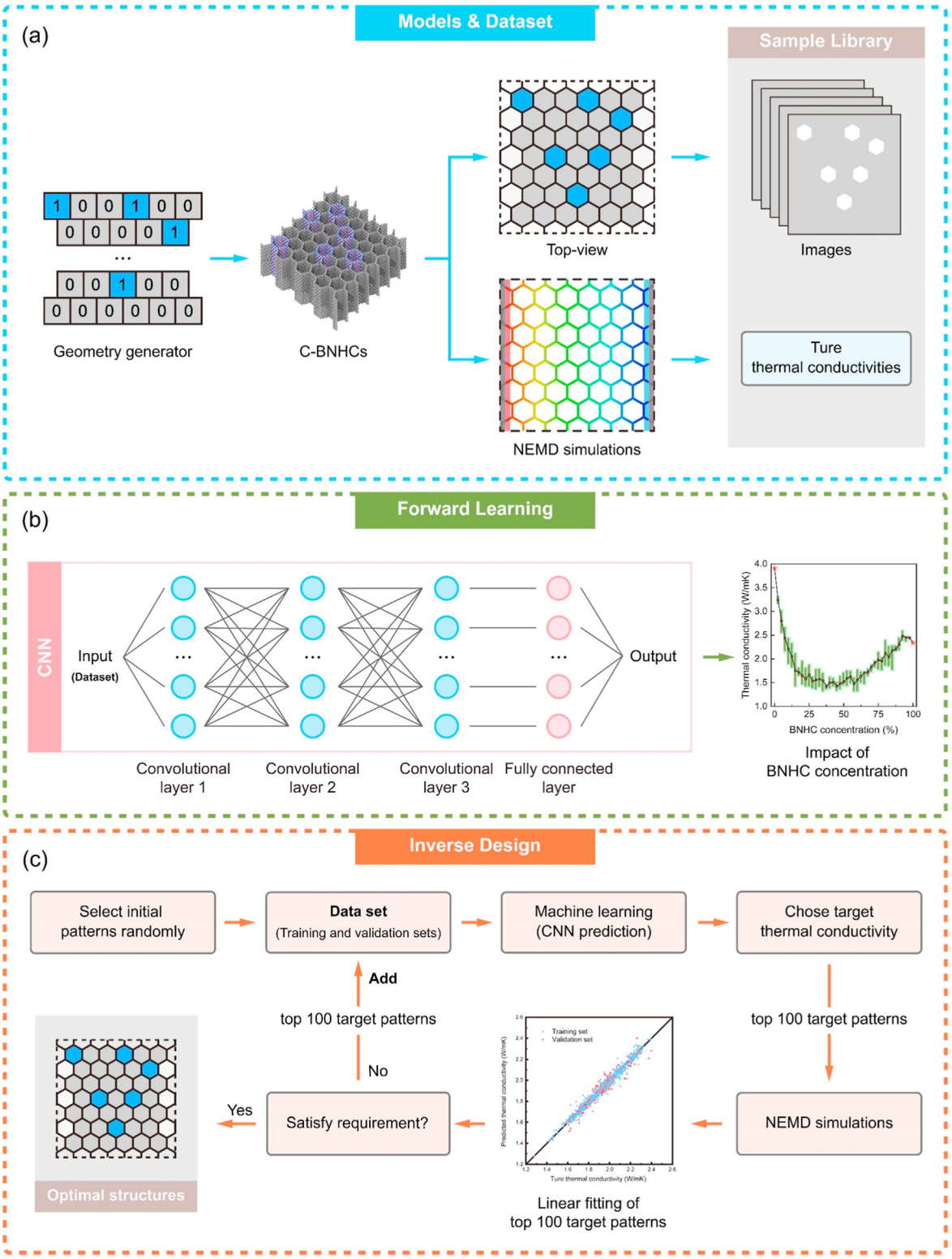

Fig. 1. The workflow of ML-based method proposed here. (a) Models and dataset construction, which include the generation of numerous C–BNHC structures, and assembly of the C–BNHC sample patterns and their thermal conductivities to establish the sample library. (b) Forward learning based on the CNN model, which is employed to explore the relation between BNHC concentration and thermal conductivity of C–BNHCs. The inset shows the architecture of defined CNN model. (c) Inverse design, which contains a series of evolutionary steps for searching optimal C–BNHC structures possessing required thermal conductivity. (A colour version of this figure can be viewed online.)

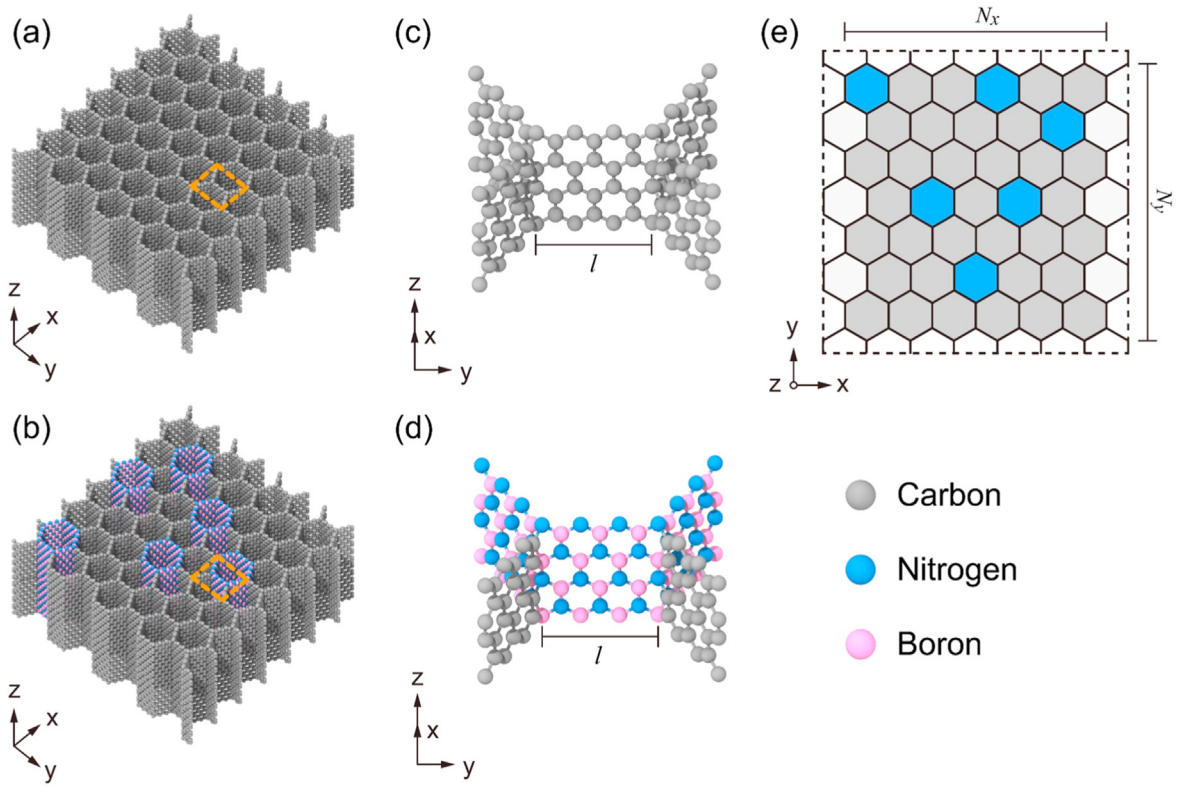

Fig. 2. Schematics of (a) a pure CHC structure and (b) a hybrid C–BNHC structure. The junction configurations in (c) CHCs and (d) C–BNHCs, which correspond to the yellow dotted regions in (a) and (b). Here, gray, blue and pink balls indicate carbon, nitrogen and boron atoms, respectively. (e) The top-view of the C–BNHC structure shown in (c). The gray and blue hexagons represent CHC and BNHC cells, respectively. (A colour version of this figure can be viewed online.)

In the present study, we mainly focus on the in-plane thermal transport property of C–BNHCs. Thus, to simplify our analysis, the C–BNHC structure was equivalently simplified into a 2D model. The corresponding 2D top-view patterns of 3D C–BNHCs as shown in Fig. 2(e) can be treated as the input images in the CNN model. Here, the rectangular C–BNHC samples considered have a size of $N_x \times N_y$ cells, where N_x and N_y denote numbers of honeycomb cells in x and y directions, respectively. Here, all cells except those near the boundaries in C–BNHCs can be treated as the designable candidate blocks. Thus, the total number of possible doping BNHC cell candidates is $N_c = N_x \times N_y - \lfloor N_y/2 \rfloor$, where $\lfloor \ldots \rfloor$ denotes the floor function and N_y is an odd number. When the number of doping BNHC cells is fixed as N_d, a series of C–BNHCs containing $N_c!/[N_d! \cdot (N_c - N_d)!]$ possible different patterns can be constructed by the random geometry generator. It is noted here that C–BNHCs with the similar (or symmetric) structures are also considered here, because this treatment can make the trained ML model have the ability to distinguish the similar structures of C–BNHCs, which will thus enhance the reliability and accuracy of the defined ML model.

In this work, we considered two simulation samples with same length in z direction of 21.30 Å. One is the sample with a size of 5×5 cells (76.68×66.41 Å^2) as shown in Fig. S1. This sample was adopted to validate the stability and reliability of the present ML-based method, since we can enumerate all results via conventional method due to its relatively small size. The other one is a larger model with a size of 6×7 cells (89.46×88.54 Å^2) as shown in Fig. 2(b), which was employed to further investigate the effect of BNHC concentration and arrangement on the thermal conductivity of C–BNHCs. Here, the total numbers of atoms in the small and large C–BNHC systems are 6120 and 9520, respectively. The size selected here for C–BNHC systems can result in a steady temperature distribution in C–BNHC and thus a reliable thermal conductivity from NEMD simulations (see Fig. S4 in the Supplementary Materials). In addition, as shown in Table S1 (see the Supplementary Materials), almost no significant changes are found in the dimensions of C–BNHCs with different BNHC concentrations.

2.3. NEMD simulations

In the ML-based method, an essential and initial step is to construct the dataset. A series of C–BNHC structures has been built by the above approach, then it is supposed to calculate each thermal conductivity of them. Here, the NEMD simulations were performed to estimate thermal conductivity of C–BNHCs with the aid of open-source package LAMMPS [62]. For the sake of predicting the thermal property of C–BNHC systems accurately, the covalent bonding among C, B and N atoms was described by the optimized Tersoff potential [63]. Since it can describe the phonon thermal transport response better, the optimized Tersoff potential has been successfully applied in many studies on researching the thermal transport property of various carbon and BN nanomaterials [36,37,64,65].

To perform NEMD simulations, as shown in Fig. 3(a), the whole C–BNHC structure is divided into five regions along the x direction: two fixed regions at both ends, hot and cold regions (heat source and sink) adjacent to the fixed regions, and a free region between heat sink and heat source. Here, the fixed, hot and cold regions have the same length of 5 Å. After that, a heat flux (J) can be generated between the hot and cold regions, which results in a temperature gradient (dT/dx) in the middle free region. Here, the heat flux equals to the thermal energy passing along the x direction of C–BNHCs per unit time, the expression of which will be given later. In addition, the periodic boundary condition was applied in the z direction, while non-periodic boundary conditions were applied in

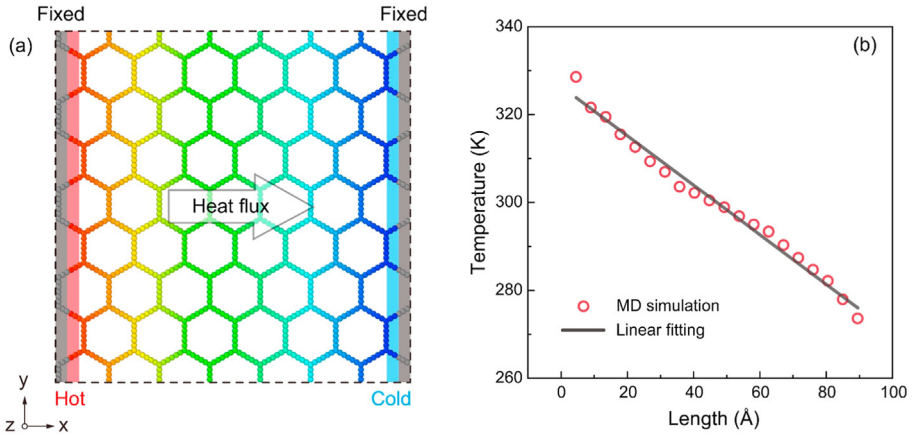

Fig. 3. (a) The NEMD simulation set-up for the thermal conductivity calculation. (b) The typical temperature distribution in C–BNHCs obtained from NEMD simulations at 300 K. (A colour version of this figure can be viewed online.)

the *x* and *y* directions to simulate a C–BNHC with the finite in-plane size.

Under the above implements, the NEMD simulations were performed with the following procedure. First, the initial configuration of a C–BNHC was relaxed to its energy-minimized sate based on the conjugate gradient method. Second, the structure was relaxed again within the isothermal-isobaric (NPT) ensemble at room temperature (300 K) and zero external pressure for 100 ps. Here, the velocity Verlet algorithm with a time step of 1 fs was utilized to integrate the Hamilton equations of motion determined by Newton's second law. Third, a Nosé-Hoover thermostat in the canonical (NVT) ensemble was performed to the system at 300 K for another 100 ps. As shown in Figs. S3(a)–S3(c), the energy, pressure and temperature of the C–BNHC reach the steady values, which indicates that the system is in the equilibrium state after the structural relaxation. Fourth, the temperatures of hot and cold regions were retained steadily at 330 K and 270 K by using a Langevin thermostat within the microcanonical (NVE) ensemble for 200 ps, which can be verified by Fig. S3(d) shown in the Supplementary Materials. In addition, as shown in Figs. S4(b) and S5(b), this temperature difference can result in a reliable temperature distribution and thus a reliable thermal conductivity from NEMD simulations. Last, the simulations continue for 1 ns under the conditions similar to the previous step. The energy exchange between the hot and cold regions thus can generate a heat flux in the middle free region. Meanwhile, the middle free region of C–BNHC was divided into 20 slabs along the heat flux direction. The temperature distribution in the C–BNHCs were thus evaluated by calculating the average temperature of each slab. As shown in Fig. 3(b), a stable linear temperature distribution along the *x* direction can be observed in the C–BNHCs.

In this study, the following equation was employed to calculate the heat flux (J) along the *x* direction [66]:

$$J = \frac{1}{A_c}\frac{\mathrm{d}E_a}{\mathrm{d}t}, \tag{1}$$

where E_a is the accumulated energy, A_c is the cross-sectional area of C–BNHCs and t is the simulation time. During NEMD simulations, a constant amount of energy ($\mathrm{d}E_a$) is added to the hot region at each timestep ($\mathrm{d}t$). Meanwhile, the same amount of energy should be removed from the cold region. Here, the accumulated energy can be represented by the summation of the kinetic and potential energies:

$$E_a = \sum_i^N \left(\frac{1}{2}m_i v_i^2 + \phi_i\right), \tag{2}$$

where m_i, v_i and ϕ_i are the mass, velocity and potential energy of atom i, respectively, and N is the total atom number of the system. After averaging the accumulated energy of hot and cold regions within a period of simulation time in NEMD simulations, the heat flux can be calculated from Eq. (1). Moreover, the average temperature of the ith slab (T_i) can be calculated by Ref. [67]:

$$T_i = \frac{2}{3N_i K_B}\sum_j^{N_i}\frac{p_j^2}{2m_j}, \tag{3}$$

where p_j and m_j are the momentum and atomic mass of the jth atom, respectively, N_i is the number of atoms in the ith slab, and K_B is the Boltzmann constant. Thus, after obtaining the heat flux from Eq. (1) and the temperature distribution from Eq. (3) in NEMD simulations, the thermal conductivity (κ) of C–BNHCs can be computed according to the following Fourier's law [66]:

$$\kappa = \frac{J}{\mathrm{d}T/\mathrm{d}x}. \tag{4}$$

2.4. ML-based optimization procedures

The performance of forward learning and inverse design based on the ML method strongly relies on an efficient and reliable deep neural network. Hence, a CNN model modified based on the VGGNet [61] was constructed for predicting the thermal transport property of C–BNHCs. As plotted in Fig. 1(b), the architecture of CNN model considered here is comprised of four parts: an input layer (the dataset), three convolutional layers (CLs), a fully connected layer (FL), and an output layer. All data in the input layer was randomly divided into two parts. Specifically, 90% data was selected to train the CNN model (training set), while the remaining 10% data was used to validate the trained CNN model (validation set). Each data considered here contains two parts: a grayscale image of size 56×56 pixels representing the top-view schematic of C–BNHC, and a label illustrating the corresponding true thermal conductivity calculated via NEMD simulations. Then, each CL was successively followed by a batch normalization layer, a rectified linear unit (ReLU) function and a max-pooling layer of size 2×2 with a stride of

2. It is noted that the kernel size was fixed at 3×3 with a stride of 1, while the numbers of kernel in three CLs were set as 16, 32 and 64, respectively. In FL the number of neurons was fixed at 64, in which the ReLU function was not performed. Furthermore, the batch size and the epoch number for each batch were set as 10 and 400, respectively. In the present CNN model, the entire parameter optimization was achieved by monitoring the following mean square error (MSE) between the predictions and targets with an Adam optimizer:

$$\mathrm{MSE} = \frac{1}{N_t}\sum_{i=1}^{N_t}\left(\kappa_t^i - \kappa_p^i\right)^2, \tag{5}$$

where N_t is the number of test data, κ_t^i is the true thermal conductivity of the ith test data calculated from NEMD simulations, and κ_p^i is the predicted thermal conductivity of the ith test data extracted from the ML method. A lower MSE value corresponds to a CNN model with better performance. The stability and reliability of defined CNN model will be verified later.

With the aid of constructed CNN models, as depicted in Fig. 1(b) and (c), our ML method can be employed in the forward learning the thermal conductivity of various C–BNHCs and also the inverse designing C–BNHC structures that possess required thermal conductivity. Specifically, in order to determine the thermal conductivity range of all possible C–BNHCs, it is necessary to understand the impact of BNHC concentration on the thermal transport property of C–BNHCs. Thus, the forward learning was first employed to predict the thermal conductivities of a group of C–BNHC structures possessing random doping distribution and concentration. In doing this, a small part of the constructed C–BNHC samples was tested in NEMD simulations to calculate their thermal conductivities. These C–BNHCs together with their values of thermal conductivities were utilized as the ML dataset to be fed into the optimized CNN model. After predicting the thermal conductivities of the rest unexplored C–BNHCs in sample library, the relation between the BNHC concentration and thermal conductivity of C–BNHCs can be obtained as shown in Fig. 1(b). Based on the results obtained from the above forward learning, value range of thermal conductivity of C–BNHCs with different BNHC concentrations can be observed as well. Accordingly, we can determine the number of doping cells N_d according to the desired thermal conductivity of C–BNHCs.

After determining the value range of thermal conductivity of various C–BNHCs, the inverse design strategy as shown in Fig. 1(c) was performed to discover the optimal C–BNHC structures with required thermal conductivity. Here, in order to establish another sample library (or design space), a new group of C–BNHC structures with the determined number of doping cells N_d was constructed. For increasing the possibility for finding optimal structures, the sample library volume was much larger than that in the prior forward learning process. At the beginning of the ML-based inverse design process, 100 C–BNHC structures were randomly selected from the new sample library, whose thermal conductivities were then calculated from NEMD simulations. Their patterns and thermal conductivities thus constructed an initial dataset for the whole inverse design process, i.e., the first generation of structure optimization. Afterwards, based on NEMD simulations and ML predictions, the modification of thermal conductivity of C–BNHCs was achieved according to the following evolutionary procedures [see in Fig. 1(c)]. (1) The dataset was fed into the CNN model to learn the relation between spatial location and thermal conductivity κ of C–BNHCs. (2) The trained CNN model with high accuracy was established, which was used to predict the thermal conductivities of untrained patterns in sample library. (3) According to the predicted information and the required value of κ, we selected the top 100 target patterns, which were considered in NEMD simulations to calculate true κ. (4) If the top 100 target structures satisfied our requirement, the results showing the regression performance of the ML-based inverse design was plotted as a scatter graph. The optimal structures were thus determined at the end. (5) If the structures did not satisfy our requirement, the calculated κ of top 100 target structures and their patterns in current iteration would be added into the prior dataset as a new input dataset of CNN model in the next iteration, resulting in the continuous expansion on the volume of dataset during the inverse design process. The optimization and discrimination procedures were continued until the selected top 100 patterns satisfied our requirements.

3. Results and discussion

3.1. Model and method validation

Before studying the thermal conductivity of C–BNHCs, we should verify the thermodynamic stability of the constructed C–BNHCs and, meanwhile, validate the accuracy the present ML-based method. As shown in Fig. S2, a unit cell containing junctions comprised of one graphene nanoribbon and two BN nanoribbons was employed here to equivalently represent the hybrid C–BNHC structure, which has 64 atoms. The thermodynamic stability of the proposed C–BNHC system was examined by ab initio molecular dynamics (AIMD) simulations with the aid of Vienna ab initio simulation package (VASP) [68,69]. In doing this, the lattice parameter optimization was firstly performed for the initially constructed C–BNHC unit cell. Afterwards, a 2×2×2 supercell containing 544 atoms was relaxed within the NVT ensemble at 1000 K by using Andersen thermostat for 50 ps. Here, the timestep was selected as 2 fs, while the width of Gaussian smearing was selected as 0.1 eV. The gamma-point scheme with 1×1×1 mesh was applied in our AIMD simulations. As shown in Fig. 4, the total energy of the supercell of the C–BNHC reaches equilibrium rapidly at the beginning of AIMD simulations and remains almost unchanged afterwards. Moreover, despite some slight distortions of

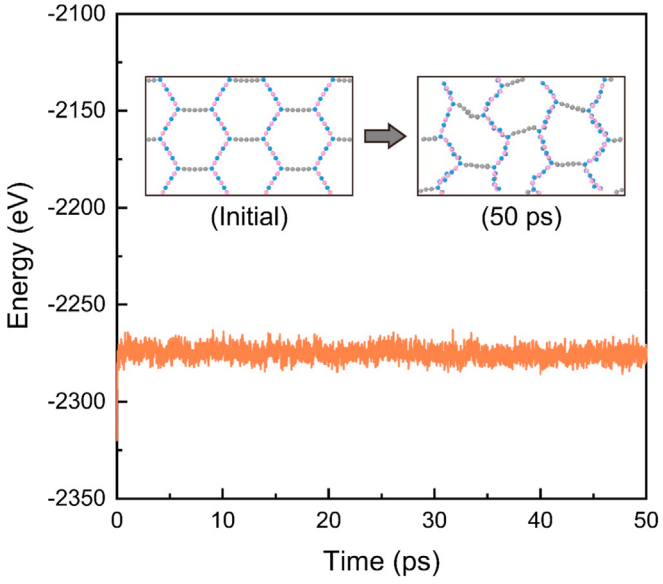

Fig. 4. Total energy of a 2×2×2 supercell of C–BNHC at 1000 K calculated by AIMD simulations. The insets show the structure of C–BNHC before and after the simulation. Here, gray, blue, and pink balls represent carbon, nitrogen and boron atoms, respectively. (A colour version of this figure can be viewed online.)

atoms due to large thermal movements at high temperature, no bond breakages or disorders are found in the atomic structures of C–BNHCs after AIMD simulations. In other words, when compared with the initial configuration, no topological change is observed during the entire AIMD simulation process. These findings demonstrate the thermodynamic stability of the proposed C–BNHC structures, which, to some extent, indicates that the similar C–BNHCs can be achievable in experiments.

To evaluate the reliability and efficiency of the proposed ML-based methods, as mentioned in Sec. 2.4, we enumerated all possible structures of C–BNHCs having a relatively small size of 5×5 cells (see in Fig. S1) and containing three doping BNHC cells, i.e., $N_d = 3$. Thus, 1771 different patterns of C–BNHCs were considered in the sample library. We directly compared the thermal conductivities of all C–BNHC structures calculated from NEMD simulations to the results predicted from the ML method. In doing this, the following parameter (R^2) was introduced to estimate the regression performance of CNN model:

$$R^2 = 1 - \frac{\sum_{i=1}^{N_t} \left| \kappa_t^i - \kappa_p^i \right|}{\sum_{i=1}^{N_t} \left| \kappa_t^i - \frac{1}{N_t} \sum_{i=1}^{N_t} \kappa_p^i \right|^2} \tag{6}$$

It is noted that the ML method with a R^2 closer to 1.0 exhibits a better performance.

We firstly investigated the impacts of the depth of CNN model and the number of neurons in FL to determine an optimal deep neural network architecture. Values of R^2 for different networks containing the training and validation sets are given in Fig. S6(a). Obviously, the performance of deeper CNN model "C16C32C64F*n*" is better than that of the monolayer CNN model "C64F*n*" or the pure fully connected model "F*n*". Here, "C*n*" represents a CL consisting of *n* kernels, while "F*n*" denotes an FL with *n* neurons. Furthermore, the value of R^2 is observed to be much closer to 1.0 in the deeper network with larger number of neurons in FL. Specifically, when the FL contains 64 neurons, values of R^2 are, respectively, 0.98 and 0.93 for training and validation sets, which indicate that the CNN now can be utilized to accurately predict the thermal conductivity of C–BNHCs. Under this circumstance, the "C16C32C64F64" model containing 244353 trainable parameters was selected as the deep neural network used in the present study.

After determining the optimized depth of CNN model, we then need to choose the suitable dataset size as well as the batch size and epoch number for each batch. First, we determine the batch size. When the CNN models have the same epoch number of 400 but different batch sizes, the average convergence lines of MSE (or learning curves) obtained during the training process of training and validation sets are shown in Figs. S6(c) and S6(d), respectively. It is obvious that MSE converges rapidly as the batch size increasing. Particularly, when the batch size is smaller than 10, the convergence rate will no longer increase significantly. However, the computational cost under this condition will be greatly increased. Therefore, the batch size was selected as 10 in the subsequent forward learning and inverse design procedures. In addition, the difference of MES between training and validation sets after 400 epochs is lower than 0.2%, which indicates that there is no over-fitting and under-fitting in the present CNN model. Second, we determine the epoch number. When the batch size is selected as 10, R^2 of CNN models with the epoch number increasing from 10 to 1000 is graphically shown in Fig. S6(b). The value of R^2 is found to increase initially and reach a steady value when the epoch number grows to 400. The steady values are 0.98 and 0.93 for the training and validation sets, respectively, which indicate a good performance of the present CNN models. Although we can further increase the epoch number to obtain a CNN model with higher accuracy, this treatment is not efficient for the present study because it will cause more computational cost with an extremely small increase of R^2. Hence, the epoch number was selected as 400 in our work. Last, we determine the dataset size. The MSE convergence curves of CNN models with different dataset sizes (50, 100 and 150) are shown in Figs. S6(e) and S6(f). From Fig. S6(e) we can see that the dataset size has a trivial effect on the learning curves of the training set. As shown in Fig. S6(f), in the validation set the learning performance of the CNN model with the dataset size of 100 is better than others, since its learning curve is found to converge much faster and better. Therefore, the dataset size was selected as 100 in the ML process.

In the above discussion, we have identified five important parameters in the CNN models. By randomly selecting some data as the dataset to feed into the CNN model, we optimized the trainable parameters and thus obtained the thermal conductivity of C–BNHCs from ML methods. Meanwhile, we also computed the true thermal conductivity of all C–BNHCs in the sample library directly via NEMD simulations. The linear regression between true and predicted thermal conductivities of the present C–BNHCs is shown in Fig. 5(a). As shown in this figure, values of R^2 are 0.98 and 0.93 for training and validation sets, respectively, which indicate that the developed CNN model can accurately estimate the thermal conductivity of C–BNHCs. We further employed the CNN model in the inverse design to search for the lowest and highest thermal conductivities of C–BNHC samples with the size of 5×5 cells and three doping BNHC cells. As shown in Fig. 5(b), the patterns of C–BNHCs with the lowest and highest thermal conductivities predicted from the ML method are exactly identical to those directly identified from NEMD simulations. As expected, doping BNHC cells in the C–BNHC with the lowest thermal conductivity (1.28 W/mK) are vertical towards the heat flux direction (i.e., the *x* direction), while the doping cells in the C–BNHC with the highest thermal conductivity (2.40 W/mK) are parallel to the heat flux direction. The good agreement between ML and MD methods indicates that the ML method can be treated as an accurate and efficient method to evaluate the thermal transport property of C–BNHCs. In what follows, the ML method will be further employed to study the impact of doping BNHC cells on the thermal conductivity of a relatively large C–BNHC structure and, meanwhile, utilized to design the pattern of C–BNHCs with a desired thermal conductivity.

3.2. Forward learning of the thermal conductivity

After verifying the accuracy of ML method, we employed the ML method to investigate the influence of doping BNHC cells on the thermal transport property of C–BNHC samples with a relatively large size of 6×7 cells [see in Fig. 2(b)]. In doing this, the thermal conductivity of C–BNHCs with the random arrangement and concentration of doping BNHC cells was predicted from the CNN model defined above. The obtained results are graphically shown in Fig. 6(a). It is found that the doping BNHC can significantly reduce the thermal conductivity of C–BNHCs. In general, the reduction of thermal conductivity observed in C–BNHCs mainly originates from the following two factors. First, the thermal conductivity of BNHCs is smaller than that of CHCs. Thus, the thermal conductivity of C–BNHCs is expected to range between the values of CHCs and BNHCs. Second, due to the heterostructure of C–BNHCs, the phonon scattering in these hybrid systems is expected to be more significant than that in pure CHCs and BNHCs, which can reduce the thermal transport property. To figure out whether the phonon scattering is indeed more significant in the present C–BNHCs, we compared the phonon density of states (PDOS) of all atoms in CHC,

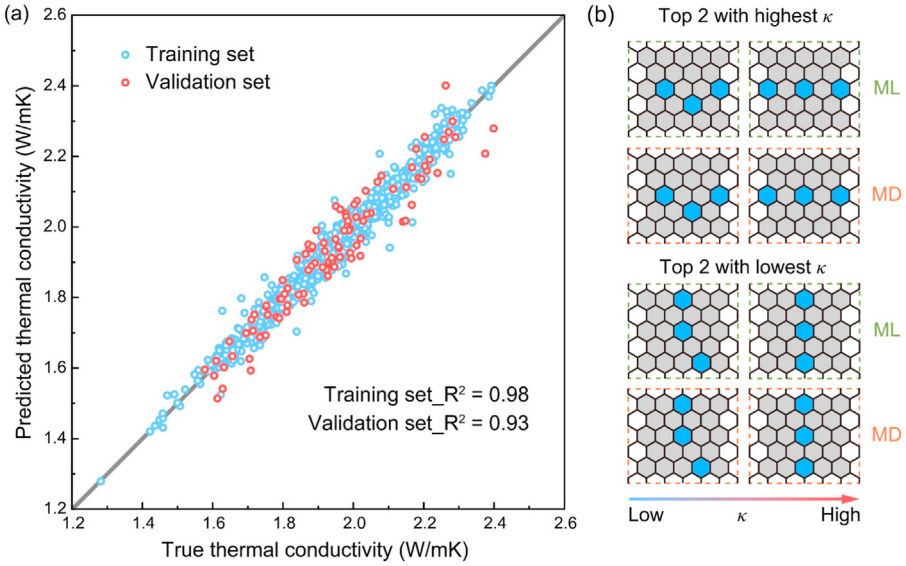

Fig. 5. (a) The linear regression between true and predicted thermal conductivities κ. (b) The optimal patterns of C–BNHCs extracted from ML prediction and MD simulations. The up and bottom panels show the top 2 target patterns of C–BNHCs with the highest and lowest κ, respectively. (A colour version of this figure can be viewed online.)

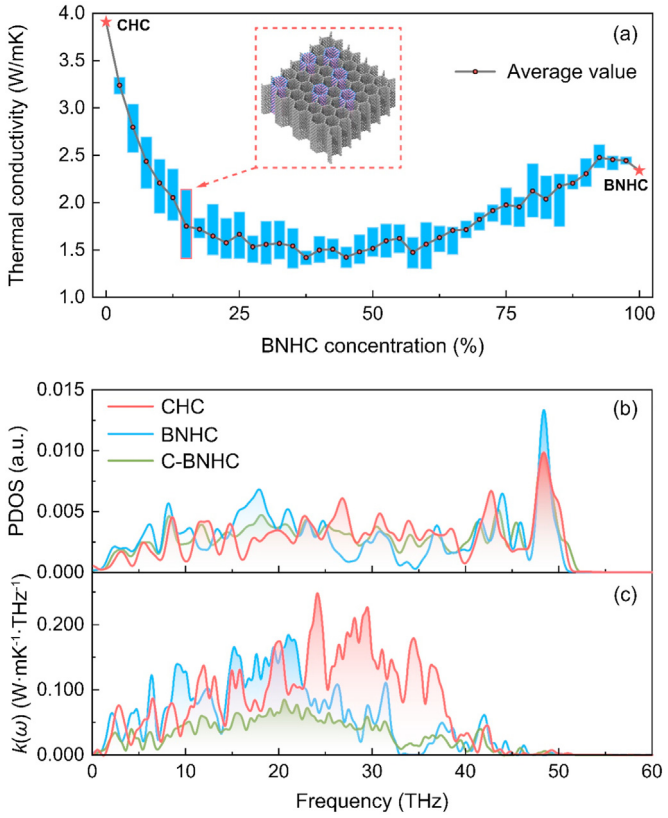

Fig. 6. (a) Thermal conductivities of C–BNHCs with different BNHC concentrations. The red stars represent the thermal conductivities of pure CHCs and BNHCs. The inset shows the representative structure of C–BNHC containing 6 doping BNHC cells considered in the inverse design. (b) The calculated PDOS patterns and (c) spectral thermal conductivities of CHC, BNHC and C–BNHC containing 50% doping BNHC cells. (A colour version of this figure can be viewed online.)

BNHC and C–BNHC systems. Here, the PDOS was calculated by applying the following Fourier transformation to the atomic velocity autocorrelation functions at equilibrium state within the NVE ensemble [70]:

$$\mathrm{PDOS}(\omega) = \int \frac{\left\langle \sum_{j=1}^{N} \boldsymbol{v}_j(t_0) \cdot \boldsymbol{v}_j(t_0 + t) \right\rangle}{\left\langle \sum_{j=1}^{N} \boldsymbol{v}_j(t_0) \cdot \boldsymbol{v}_j(t_0) \right\rangle} \cdot \exp(-2\pi i \omega t) \mathrm{d}t \qquad (7)$$

where ω is the phonon frequency, $\boldsymbol{v}_j(t_0)$ and $\boldsymbol{v}_j(t_0+t)$ represent the velocities of the jth atom at the initial time t_0 and the current time t_0+t of each calculation, respectively, and <…> means an atom number-averaged velocity autocorrelation function. To obtain the final PDOS patterns, 9000 parallel simulations were performed. Here, the timestep, the correlation time and the total simulation time in the simulation were chosen as 1 fs, 1 ps and 10 ps, respectively. The convergence lines of velocity autocorrelation functions of different systems are shown in Fig. S7. It is found that the velocity autocorrelation function can converge to zero after the simulation with the chosen correlation time of 1 ps, which indicates the reliability of the obtained PDOS.

In Fig. 6(b) we show the PDOS of the C–BNHC with the BNHC doping concentration being 50%. For the sake of comparison, PDOS patterns of the pure CHC and BNHC are also shown here. In the low frequency range of 0–20 THz, the PDOS of BNHC generally is slightly higher than that of CHC and C–BNHC. In the middle frequency range of 20–40 THz, the CHC is generally found to have the highest PDOS among three materials. Although the high frequency peaks of CHC, BNHC and C–BNHC all locate around 48 THz, the amplitude of BNHC is much higher than that of CHC and C–BNHC. From this figure, we also see that when compared with pure CHC and BNHC, fewer frequency peaks are observed in the PDOS of C–BNHC. In other words, the PDOS pattern of C–BNHC is much smoother than that of CHC and BNHC.

To better clarify the effect of phonon frequency on the thermal conductivity of the C–BNHC, we also calculated its spectral thermal conductivity $k(\omega)$ with the aid of GPUMD package [71]. Details about the calculation of spectral thermal conductivity are shown in the Supplementary Materials. The obtained result is shown in Fig. 6(c). For the sake of comparison, the corresponding results of CHC and BNHC are also shown in this figure. It is found that the high frequency phonons larger than 40 THz almost have no effects on

the thermal conductivity of CHC, BNHC and C–BNHC. The thermal transport in CHC is found to be mainly induced by the phonon vibration in the range of 10–40 THz. As for the BNHC, the phonon vibration in the range of 10–20 THz majorly determines its thermal transport property. Similar to the CHC, the thermal transport in C–BNHC is dominated by the phonon vibration in the range of 10–40 THz. However, $k(\omega)$ of C–BNHC is apparently lower than that of pure CHC and BNHC, which means that the C–BNHC containing 50% doping BNHC cells should possess a thermal conductivity smaller than that of CHC and BNHC. The above findings, to some extent, indicate that more phonon scattering indeed exists in C–BNHCs, which is thus a factor possibly responsible for the reduction of their thermal conductivity as shown in Fig. 6(a).

Furthermore, from Fig. 6(a) we can also see that the thermal conductivity of C–BNHCs strongly depends on both the arrangement and concentration of doping BNHC cells. For example, when the concentration of doping BNHC cells is 15%, the thermal conductivity κ of C–BNHCs with different arrangements of BNHC cells ranges from 1.41 W/mK to 2.14 W/mK. With increasing the concentration of doping BNHC cells, a nonmonotonic change is found in the averaged κ of C–BNHCs with different arrangements of BNHC cells. Specifically, the averaged κ is found to decrease from 3.92 W/mK at the concentration of zero (pure CHCs) to 1.58 W/mK at the concentration of 50%. However, when the concentration keeps increasing from 50% to 100% (pure BNHCs), the averaged κ is found to be enhanced by 32%. The similar nonmonotonic relation between the thermal conductivity and the doping concentration is also observed in other hybrid C-BN nanomaterials such as 2D graphene-BN heterostructures [36,64]. The nonmonotonic relation between the thermal conductivity and doping concentration can be explained by the nonmonotonic change of phonon scattering in the C–BNHCs with varied doping concentration of BNHC cells. It is noted that the maximum degree of material hybridization occurs at the C–BNHCs with 50% doping BNHC cells, which thus have the most significant phonon scattering. Thus, with further increasing the doping concentration of BNHC cells after 50%, the phonon scattering in C–BNHCs oppositely decreases, which results in the increase of thermal conductivity of C–BNHCs in this process.

3.3. Inverse design of C–BNHC structure

In addition to directly predicting the thermal conductivity of C–BNHCs with different arrangements and concentrations of doping BNHC cells, the ML method proposed here also can be utilized to inversely design the pattern of C–BNHCs with a desired thermal conductivity. As an example, in what follows, we employed the ML-based evolutionary method to design C–BNHCs with four specific thermal conductivities including the highest value, the lowest value, and two random values (1.7 W/mK and 2.0 W/mK). Similar to the above discussion, a large C–BNHC structure with a size of 6×7 cells was considered here, which contained 39 candidate doping cells as shown in Fig. 2(b). According to the aforementioned requirements of thermal conductivity and the results derived from the above forward learning, the number of the doping BNHC cells N_d was selected as 6, which led to more than three million possibilities in total. Among these massive possible patterns, 10^4 different patterns were randomly selected to generate our sample library of inverse design.

As plotted in Fig. 7(a), the averaged thermal conductivity κ of top 100 target structures for each iteration is involved to demonstrate the inverse design procedure. In searching the structures possessing the highest and lowest κ, values of the averaged κ are found to converge after about 6 iterations, which means that our CNN model has found the optimal structures for the highest and lowest κ of C–BNHCs. In each iteration, we ignored the patterns that have been already calculated in NEMD simulations to increase the computational efficiency. Under this circumstance, in searching the target structures, the thermal conductivity of only ~5% patterns within the total sample library were calculated from NEMD simulations, while the value of other ~95% samples were predicted by the ML method. In Fig. S8, we list the top 5 optimal C–BNHC structures for the lowest and highest κ after each iteration. It can be seen that the distribution of doping BNHC cells is extremely random initially, but it evolves to be regular rapidly during the inverse design. The obtained optimal patterns of the target C–BNHCs are also shown in Fig. 7(f). In general, it is found that the doping cells are perpendicular and parallel to the heat flux direction for the C–BNHCs possessing the lowest and highest κ, respectively. The highest thermal conductivity of 2.69 W/mK observed in the present C–BNHCs is twice higher than the lowest thermal conductivity of 1.31 W/mK, though it is 31% smaller than the value of pure CHCs. In addition, the training results predicted at the last iteration in ML method are also compared to the results computed by NEMD simulations [see in Fig. 7(b) and (c)]. It is observed that the CNN model exhibits a good regression performance at the local region near the target value. The above results indicate that the proposed ML-based optimization technique is reliable and efficient in searching certain C–BNHC structures with the specific thermal transport property.

To further verify whether the patterns of C–BNHCs with the highest and lowest κ predicted from the ML method are reliable and, meanwhile, explain why these patterns have the highest and lowest κ, in Fig. 8 we show the temperature distributions in these optimal structures. In the C–BNHCs with the highest κ, the doping BNHC cells are generally parallel to the heat flux direction. In this way, most heat still can transport through the contiguous CHC cells. As a result, this pattern is thus expected to possess the highest κ, since the thermal transport property of CHCs is better than that of BNHCs. Indeed, as shown in Fig. 8(a), no significant temperature concentration is found in this pattern and an almost linear and uniform temperature distribution is observed in the entire C–BNHC structure. In the C–BNHCs with the lowest κ, the doping BNHC cells are generally perpendicular to the heat flux direction. Thus, the heat flux can be greatly halted behind these doping BNHC cells. Indeed, as shown in Fig. 8(b), due to the existence of impediment to the heat flux, strong temperature concentrations are observed near the doping BNHC cells.

Afterwards, we employed the ML method to search the C–BNHC structures with two randomly selected thermal conductivities, i.e., κ = 1.7 and 2.0 W/mK. The iteration process for searching the optimal structures is also depicted in Fig. 7(a). It is observed that the averaged κ rapidly reaches the steady values of 1.7 and 2.0 W/mK both after 4 iterations approximately. In Fig. 7(d) and (e), we show the true thermal conductivities of these optimal structures of C–BNHCs after the last iteration, which are mostly close to the target values. The top 3 optimal structures of C–BNHCs with κ of 1.7 and 2.0 W/mK after the last iteration are illustrated in Fig. 7(f).

Finally, to estimate the relative reliability of optimal structures of C–BNHCs with the above target thermal conductivities (maximum value, minimum value, 1.7 W/mK and 2.0 W/mK), we computed their binding energies and compared the obtained results with the values of pure CHCs. Here, all results shown in Fig. S9 were obtained from MD simulations with the optimized Tersoff potential [63]. It is found that the binding energy per atom of C–BNHCs generally is only around 0.05 eV/atom higher than that of CHCs and a relatively smaller binding energy can be observed in the C–BNHCs with the tighter arrangement of doping BNHC cells. This small binding energy existing in the optimal structures of C–BNHCs proves the stability of their structures, which thus can be possibly synthesized in experiments. According to above results, we can

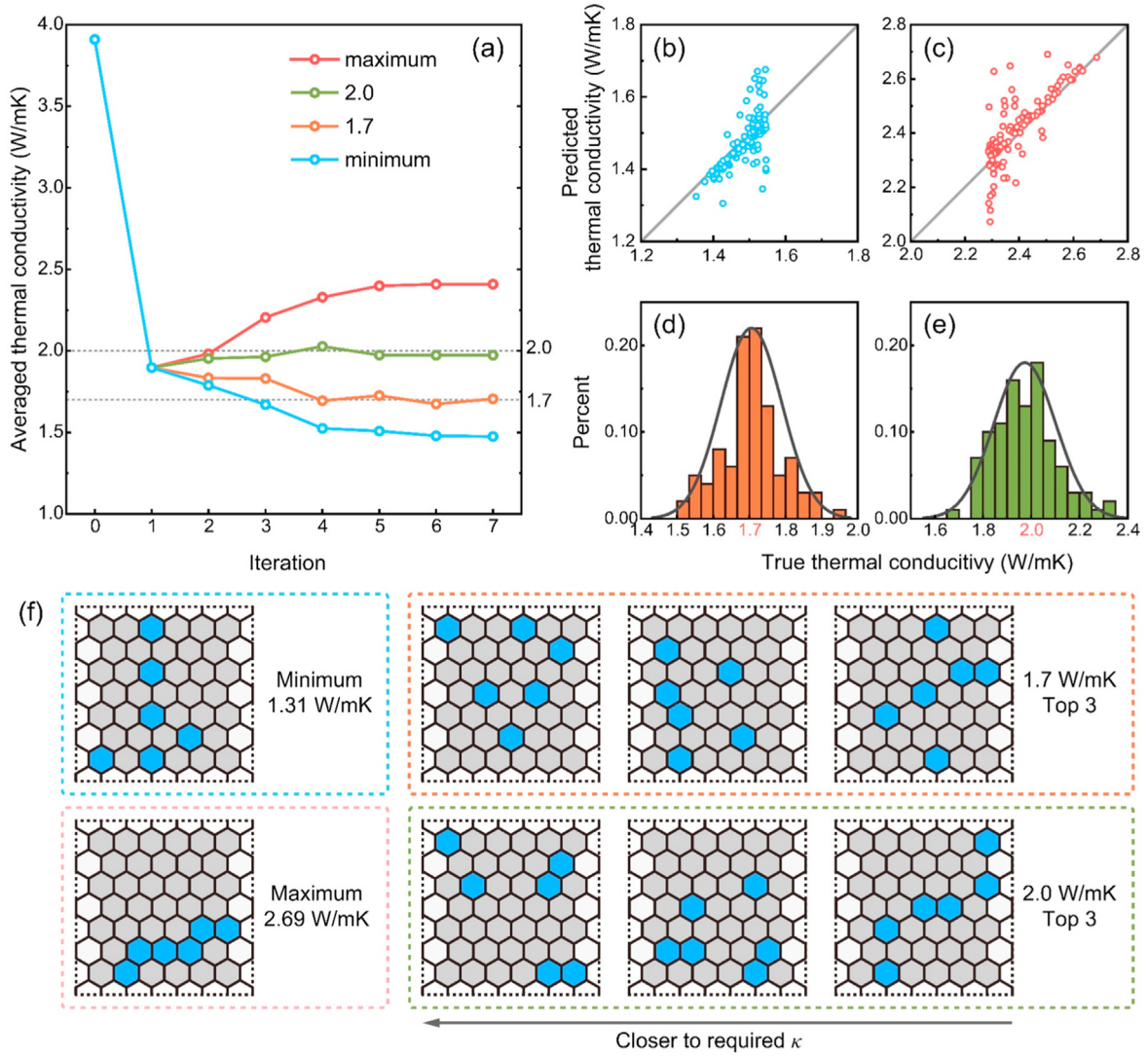

Fig. 7. The structural optimization results of C–BNHC structure with a size of 6×7 cells. (a) Averaged thermal conductivity κ of top 100 target patterns in each iteration during the inverse design. The linear regression between the true and predicted (b) lowest and (c) highest κ in the last iteration. The percent statistics of predicted structures with true κ of (d) 1.7 W/mK and (e) 2.0 W/mK. (f) The optimal C–BNHC structures with the lowest κ, highest κ, and two randomly selected κ (1.7 and 2.0 W/mK). (A colour version of this figure can be viewed online.)

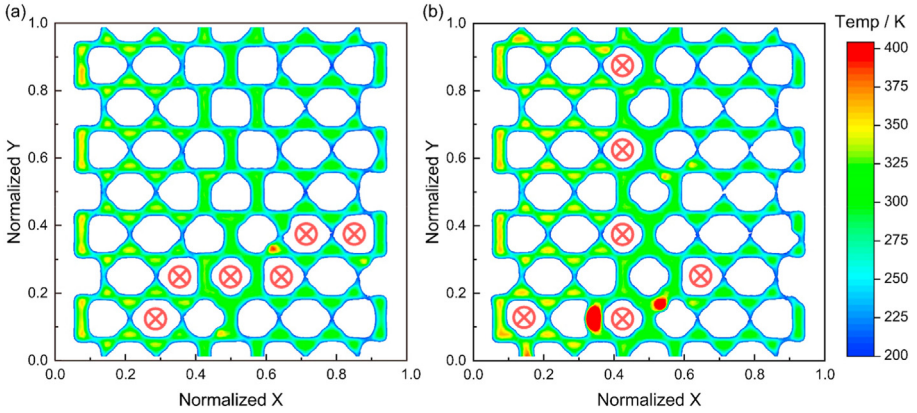

Fig. 8. The temperature distributions of optimal C–BNHC structures with (a) the highest and (b) lowest κ, in which the symbol indicates the location of doping BNHC cells. (A colour version of this figure can be viewed online.)

come to the conclusion that the present ML method is good at designing C–BNHC structures with desired thermal transport properties efficiently, accurately and practically.

4. Conclusions

In summary, a method combing the classical MD simulations and emerging ML algorithms is proposed in this work to forward study the impact of doping BNHC cells on the thermal transport property of hybrid C–BNHCs and also to inverse design the structures of C–BNHCs with specific thermal conductivities. Specifically, through the forward learning, it is found that when the BNHC doping concentration is same, the difference among thermal conductivities of C–BNHCs with different arrangements of BNHC cells can be extremely large. In addition, a nonmonotonic relation is observed between the thermal conductivity of C–BNHCs and their BNHC doping concentration, which is attributed to the complicated phonon scattering behaviors in C–BNHCs. Moreover, the present ML-based method also can be served as an accurate and effective inverse design method for designing the structures of C–BNHCs with specific thermal conductivities such as the minimum, the maximum or any other intermediate values. As for a target thermal conductivity, numerous potential optimal structures of C–BNHCs can be proposed by the present ML-based inverse design method at once. Overall, the present work not only significantly expands current knowledge of the thermal transport property of hybrid C–BNHCs, but also provides an efficient material design method for tailoring the material properties of nanohoneycombs.

CRediT authorship contribution statement

Yao Du: Conceptualization, Methodology, Software, Investigation, Validation, Formal analysis, Writing – original draft, Writing – review & editing. **Penghua Ying:** Data curation, Software, Formal analysis. **Jin Zhang:** Conceptualization, Formal analysis, Resources, Writing – review & editing, Supervision, Project administration, Funding acquisition.

Declaration of competing interest

The authors declare that they have no known competing financial interests or personal relationships that could have appeared to influence the work reported in this paper.

Acknowledgments

This work was supported by the National Natural Science Foundation of China (Grant No. 11602074) and the Natural Scientific Research Innovation Foundation in Harbin Institute of Technology (Grant No. HIT.NSRIF.2020058). JZ also acknowledges the financial support from the Harbin Institute of Technology (Shenzhen Graduate School) through the Scientific Research Starting Project for New Faculty.

Appendix A. Supplementary data

Supplementary data to this article can be found online at https://doi.org/10.1016/j.carbon.2021.08.035.

References

[1] S. Iijima, Helical microtubules of graphitic carbon, Nature 354 (1991) 56–58, https://doi.org/10.1038/354056a0.
[2] N.G. Chopra, R.J. Luyken, K. Cherrey, V.H. Crespi, M.L. Cohen, S.G. Louie, A. Zettl, Boron nitride nanotubes, Science 269 (1995) 966–967, https://doi.org/10.1126/science.269.5226.966.
[3] K.S. Novoselov, A.K. Geim, S.V. Morozov, D. Jiang, Y. Zhang, S.V. Dubonos, I.V. Grigorieva, A.A. Firsov, Electric field effect in atomically thin carbon films, Science 306 (2004) 666–669, https://doi.org/10.1126/science.1102896.
[4] K.S. Novoselov, D. Jiang, F. Schedin, T.J. Booth, V.V. Khotkevich, S.V. Morozov, A.K. Geim, Two-dimensional atomic crystals, Proc. Natl. Acad. Sci. U.S.A. 102 (2005) 10451–10453, https://doi.org/10.1073/pnas.0502848102.
[5] J.C. Meyer, A. Chuvilin, G. Algara-Siller, J. Biskupek, U. Kaiser, Selective sputtering and atomic resolution imaging of atomically thin boron nitride membranes, Nano Lett. 9 (2009) 2683–2689, https://doi.org/10.1021/nl9011497.
[6] M.M.J. Treacy, T.W. Ebbesen, J.M. Gibson, Exceptionally high Young's modulus observed for individual carbon nanotubes, Nature 381 (1996) 678–680, https://doi.org/10.1038/381678a0.
[7] J.P. Lu, Elastic properties of carbon nanotubes and nanoropes, Phys. Rev. Lett. 79 (1997) 1297–1300, https://doi.org/10.1103/PhysRevLett.79.1297.
[8] S. Berber, Y.-K. Kwon, D. Tománek, Unusually high thermal conductivity of carbon nanotubes, Phys. Rev. Lett. 84 (2000) 4613–4616, https://doi.org/10.1103/PhysRevLett.84.4613.
[9] V. Popov, Carbon nanotubes: properties and application, Mater. Sci. Eng. 43 (2004) 61–102, https://doi.org/10.1016/j.mser.2003.10.001.
[10] M.F.L. De Volder, S.H. Tawfick, R.H. Baughman, A.J. Hart, Carbon nanotubes: present and future commercial applications, Science 339 (2013) 535–539, https://doi.org/10.1126/science.1222453.
[11] C. Lee, X. Wei, J.W. Kysar, J. Hone, Measurement of the elastic properties and intrinsic strength of monolayer graphene, Science 321 (2008) 385–388, https://doi.org/10.1126/science.1157996.
[12] A.A. Balandin, S. Ghosh, W. Bao, I. Calizo, D. Teweldebrhan, F. Miao, C.N. Lau, Superior thermal conductivity of single-layer graphene, Nano Lett. 8 (2008) 902–907, https://doi.org/10.1021/nl0731872.
[13] J.H. Seol, I. Jo, A.L. Moore, L. Lindsay, Z.H. Aitken, M.T. Pettes, X. Li, Z. Yao, R. Huang, D. Broido, N. Mingo, R.S. Ruoff, L. Shi, Two-dimensional phonon transport in supported graphene, Science 328 (2010) 213–216, https://doi.org/10.1126/science.1184014.
[14] S. Bae, H. Kim, Y. Lee, X. Xu, J.-S. Park, Y. Zheng, J. Balakrishnan, T. Lei, H. Ri Kim, Y.I. Song, Y.-J. Kim, K.S. Kim, B. Özyilmaz, J.-H. Ahn, B.H. Hong, S. Iijima, Roll-to-roll production of 30-inch graphene films for transparent electrodes, Nat. Nanotechnol. 5 (2010) 574–578, https://doi.org/10.1038/nnano.2010.132.
[15] R.J. Young, I.A. Kinloch, L. Gong, K.S. Novoselov, The mechanics of graphene nanocomposites: a review, Compos. Sci. Technol. 72 (2012) 1459–1476, https://doi.org/10.1016/j.compscitech.2012.05.005.
[16] Y. Fu, J. Hansson, Y. Liu, S. Chen, A. Zehri, M.K. Samani, N. Wang, Y. Ni, Y. Zhang, Z.-B. Zhang, Q. Wang, M. Li, H. Lu, M. Sledzinska, C.M.S. Torres, S. Volz, A.A. Balandin, X. Xu, J. Liu, Graphene related materials for thermal management, 2D Mater. 7 (2019), 012001, https://doi.org/10.1088/2053-1583/ab48d9.
[17] N.G. Chopra, A. Zettl, Measurement of the elastic modulus of a multi-wall boron nitride nanotube, Solid State Commun. 105 (1998) 297–300, https://doi.org/10.1016/S0038-1098(97)10125-9.
[18] C.W. Chang, A.M. Fennimore, A. Afanasiev, D. Okawa, T. Ikuno, H. Garcia, D. Li, A. Majumdar, A. Zettl, Isotope effect on the thermal conductivity of boron nitride banotubes, Phys. Rev. Lett. 97 (2006), 085901, https://doi.org/10.1103/PhysRevLett.97.085901.
[19] A. Rubio, J.L. Corkill, M.L. Cohen, Theory of graphitic boron nitride nanotubes, Phys. Rev. B 49 (1994) 5081–5084, https://doi.org/10.1103/PhysRevB.49.5081.
[20] D. Golberg, Y. Bando, K. Kurashima, T. Sato, Synthesis and characterization of ropes made of BN multiwalled nanotubes, Scripta Mater. 44 (2001) 1561–1565, https://doi.org/10.1016/S1359-6462(01)00724-2.
[21] Y. Li, P.S. Dorozhkin, Y. Bando, D. Golberg, Controllable modification of SiC nanowires encapsulated in BN nanotubes, Adv. Mater. 17 (2005) 545–549, https://doi.org/10.1002/adma.200401266.
[22] D. Golberg, Y. Bando, Y. Huang, T. Terao, M. Mitome, C. Tang, C. Zhi, Boron nitride nanotubes and nanosheets, ACS Nano 4 (2010) 2979–2993, https://doi.org/10.1021/nn1006495.
[23] K. Watanabe, T. Taniguchi, H. Kanda, Direct-bandgap properties and evidence for ultraviolet lasing of hexagonal boron nitride single crystal, Nat. Mater. 3 (2004) 404–409, https://doi.org/10.1038/nmat1134.
[24] I. Jo, M.T. Pettes, J. Kim, K. Watanabe, T. Taniguchi, Z. Yao, L. Shi, Thermal conductivity and phonon transport in suspended few-layer hexagonal boron nitride, Nano Lett. 13 (2013) 550–554, https://doi.org/10.1021/nl304060g.
[25] B. Mortazavi, L.F.C. Pereira, J.-W. Jiang, T. Rabczuk, Modelling heat conduction in polycrystalline hexagonal boron-nitride films, Sci. Rep. 5 (2015) 13228, https://doi.org/10.1038/srep13228.
[26] C. Wang, J. Guo, L. Dong, A. Aiyiti, X. Xu, B. Li, Superior thermal conductivity in suspended bilayer hexagonal boron nitride, Sci. Rep. 6 (2016) 25334, https://doi.org/10.1038/srep25334.
[27] N. Ohba, K. Miwa, N. Nagasako, A. Fukumoto, First-principles study on structural, dielectric, and dynamical properties for three BN polytypes, Phys. Rev. B 63 (2001) 115207, https://doi.org/10.1103/PhysRevB.63.115207.
[28] B. Mortazavi, Y. Rémond, Investigation of tensile response and thermal conductivity of boron-nitride nanosheets using molecular dynamics simulations, Physica E 44 (2012) 1846–1852, https://doi.org/10.1016/j.physe.2012.05.007.
[29] K. Sato, H. Horibe, T. Shirai, Y. Hotta, H. Nakano, H. Nagai, K. Mitsuishi, K. Watari, Thermally conductive composite films of hexagonal boron nitride and polyimide with affinity-enhanced interfaces, J. Mater. Chem. 20 (2010)

2749, https://doi.org/10.1039/b924997d.
[30] X. Duan, Z. Yang, L. Chen, Z. Tian, D. Cai, Y. Wang, D. Jia, Y. Zhou, Review on the properties of hexagonal boron nitride matrix composite ceramics, J. Eur. Ceram. Soc. 36 (2016) 3725–3737, https://doi.org/10.1016/j.jeurceramsoc.2016.05.007.
[31] L. Ci, L. Song, C. Jin, D. Jariwala, D. Wu, Y. Li, A. Srivastava, Z.F. Wang, K. Storr, L. Balicas, F. Liu, P.M. Ajayan, Atomic layers of hybridized boron nitride and graphene domains, Nat. Mater. 9 (2010) 430–435, https://doi.org/10.1038/nmat2711.
[32] Z. Liu, L. Ma, G. Shi, W. Zhou, Y. Gong, S. Lei, X. Yang, J. Zhang, J. Yu, K.P. Hackenberg, A. Babakhani, J.-C. Idrobo, R. Vajtai, J. Lou, P.M. Ajayan, In-plane heterostructures of graphene and hexagonal boron nitride with controlled domain sizes, Nat. Nanotechnol. 8 (2013) 119–124, https://doi.org/10.1038/nnano.2012.256.
[33] M.P. Levendorf, C.-J. Kim, L. Brown, P.Y. Huang, R.W. Havener, D.A. Muller, J. Park, Graphene and boron nitride lateral heterostructures for atomically thin circuitry, Nature 488 (2012) 627–632, https://doi.org/10.1038/nature11408.
[34] Y. Gao, Y. Zhang, P. Chen, Y. Li, M. Liu, T. Gao, D. Ma, Y. Chen, Z. Cheng, X. Qiu, W. Duan, Z. Liu, Toward single-layer uniform hexagonal boron nitride–graphene patchworks with zigzag linking edges, Nano Lett. 13 (2013) 3439–3443, https://doi.org/10.1021/nl4021123.
[35] S.I. Kundalwal, V.K. Choyal, N. Luhadiya, V. Choyal, Effect of carbon doping on electromechanical response of boron nitride nanosheets, Nanotechnology 31 (2020) 405710, https://doi.org/10.1088/1361-6528/ab9d43.
[36] H. Sevinçli, W. Li, N. Mingo, G. Cuniberti, S. Roche, Effects of domains in phonon conduction through hybrid boron nitride and graphene sheets, Phys. Rev. B 84 (2011) 205444, https://doi.org/10.1103/PhysRevB.84.205444.
[37] S. Zhao, J. Xue, Mechanical properties of hybrid graphene and hexagonal boron nitride sheets as revealed by molecular dynamic simulations, J. Phys. D Appl. Phys. 46 (2013) 135303, https://doi.org/10.1088/0022-3727/46/13/135303.
[38] J. Zhang, C. Wang, Mechanical properties of hybrid boron nitride–carbon nanotubes, J. Phys. D Appl. Phys. 49 (2016) 155305, https://doi.org/10.1088/0022-3727/49/15/155305.
[39] F. Momeni, B. Mehrafrooz, A. Montazeri, A. Rajabpour, MD-based design of bilayer graphene-hBN heterostructures: an insight into enhanced thermal transport, Int. J. Heat Mass Tran. 150 (2020), https://doi.org/10.1016/j.ijheatmasstransfer.2019.119282, 119282.
[40] N.V. Krainyukova, E.N. Zubarev, Carbon honeycomb high capacity storage for gaseous and liquid species, Phys. Rev. Lett. 116 (2016), 055501, https://doi.org/10.1103/PhysRevLett.116.055501.
[41] N.V. Krainyukova, Capturing gases in carbon honeycomb, J. Low Temp. Phys. 187 (2017) 90–104, https://doi.org/10.1007/s10909-016-1727-1.
[42] Z. Zhang, A. Kutana, Y. Yang, N.V. Krainyukova, E.S. Penev, B.I. Yakobson, Nanomechanics of carbon honeycomb cellular structures, Carbon 113 (2017) 26–32, https://doi.org/10.1016/j.carbon.2016.11.020.
[43] X. Gu, Z. Pang, Y. Wei, R. Yang, On the influence of junction structures on the mechanical and thermal properties of carbon honeycombs, Carbon 119 (2017) 278–286, https://doi.org/10.1016/j.carbon.2017.04.054.
[44] F. Meng, C. Chen, H. Dianyin, J. Song, Deformation behaviors of three-dimensional graphene honeycombs under out-of-plane compression: atomistic simulations and predictive modeling, J. Mech. Phys. Solid. 109 (2017) 241–251, https://doi.org/10.1016/j.jmps.2017.09.003.
[45] J. Zhang, A nonlocal continuum model for the buckling of carbon honeycombs, Meccanica 53 (2018) 2999–3013, https://doi.org/10.1007/s11012-018-0854-y.
[46] Q. Qin, T. Sun, H. Wang, P. Brault, H. An, L. Xie, Q. Peng, Adsorption and diffusion of hydrogen in carbon honeycomb, Nanomaterials 10 (2020) 344, https://doi.org/10.3390/nano10020344.
[47] Y. Gao, Y. Chen, C. Zhong, Z. Zhang, Y. Xie, S. Zhang, Electron and phonon properties and gas storage in carbon honeycomb, Nanoscale 8 (2016) 12863–12868, https://doi.org/10.1039/c6nr03655d.
[48] M. Wu, X. Wu, Y. Pei, Y. Wang, X.C. Zeng, Three-dimensional network model of carbon containing only sp2-carbon bonds and boron nitride analogues, Chem. Commun. 47 (2011) 4406, https://doi.org/10.1039/c0cc05738j.
[49] Y. Wang, Y. Ding, J. Ni, Stereo boron nitride nanoribbons with junction-dependent electronic structures from first-principles, J. Phys. Chem. C 116 (2012) 5995–6003, https://doi.org/10.1021/jp2086945.
[50] J. Dai, X. Wu, J. Yang, X.C. Zeng, Unusual metallic microporous boron nitride networks, J. Phys. Chem. Lett. 4 (2013) 3484–3488, https://doi.org/10.1021/jz4018877.
[51] J. Zhang, Boron nitride honeycombs with superb and tunable piezopotential properties, Nanomater. Energy 41 (2017) 460–468, https://doi.org/10.1016/j.nanoen.2017.10.005.
[52] L. Xie, T. Wang, C. He, Z. Sun, Q. Peng, Molecular dynamics simulation on mechanical and piezoelectric properties of boron nitride honeycomb structures, Nanomaterials 9 (2019) 1044, https://doi.org/10.3390/nano9071044.
[53] H. Wang, Q. Cao, , et al.S. Liu, Atomistic study of mechanical behaviors of carbon honeycombs, Nanomaterials 9 (2019) 109, https://doi.org/10.3390/nano9010109.
[54] Z. Pang, X. Gu, Y. Wei, R. Yang, M.S. Dresselhaus, Bottom-up design of three-dimensional carbon-honeycomb with superb specific strength and high thermal conductivity, Nano Lett. 17 (2017) 179–185, https://doi.org/10.1021/acs.nanolett.6b03711.
[55] P.Z. Hanakata, E.D. Cubuk, D.K. Campbell, H.S. Park, Accelerated search and design of stretchable graphene kirigami using machine learning, Phys. Rev. Lett. 121 (2018) 255304, https://doi.org/10.1103/PhysRevLett.121.255304.
[56] P.Z. Hanakata, E.D. Cubuk, D.K. Campbell, H.S. Park, Forward and inverse design of kirigami via supervised autoencoder, Phys. Rev. Research. 2 (2020), 042006, https://doi.org/10.1103/PhysRevResearch.2.042006.
[57] J. Wan, J.W. Jiang, H.S. Park, Machine learning-based design of porous graphene with low thermal conductivity, Carbon 157 (2020) 262–269, https://doi.org/10.1016/j.carbon.2019.10.037.
[58] H. Wei, H. Bao, X. Ruan, Genetic algorithm-driven discovery of unexpected thermal conductivity enhancement by disorder, Nanomater. Energy 71 (2020) 104619, https://doi.org/10.1016/j.nanoen.2020.104619.
[59] B. Zheng, G.X. Gu, Tuning the graphene mechanical anisotropy via defect engineering, Carbon 155 (2019) 697–705, https://doi.org/10.1016/j.carbon.2019.09.008.
[60] M.A.N. Dewapriya, R.K.N.D. Rajapakse, W.P.S. Dias, Characterizing fracture stress of defective graphene samples using shallow and deep artificial neural networks, Carbon 163 (2020) 425–440, https://doi.org/10.1016/j.carbon.2020.03.038.
[61] K. Simonyan, A. Zisserman, Very Deep Convolutional Networks for Large-Scale Image Recognition, 2015. ArXiv:1409.1556 [Cs], http://arxiv.org/abs/1409.1556.
[62] S. Plimpton, Fast parallel algorithms for short-range molecular dynamics, J. Comput. Phys. 117 (1995) 1–19, https://doi.org/10.1006/jcph.1995.1039.
[63] L. Lindsay, D.A. Broido, Optimized Tersoff and Brenner empirical potential parameters for lattice dynamics and phonon thermal transport in carbon nanotubes and graphene, Phys. Rev. B 81 (2010) 205441, https://doi.org/10.1103/PhysRevB.81.205441.
[64] A. Kınacı, J.B. Haskins, C. Sevik, T. Çağın, Thermal conductivity of BN-C nanostructures, Phys. Rev. B 86 (2012) 115410, https://doi.org/10.1103/PhysRevB.86.115410.
[65] I.M. Felix, L.F.C. Pereira, Thermal conductivity of graphene-hBN superlattice ribbons, Sci. Rep. 8 (2018) 2737, https://doi.org/10.1038/s41598-018-20997-8.
[66] T. Ikeshoji, B. Hafskjold, Non-equilibrium molecular dynamics calculation of heat conduction in liquid and through liquid-gas interface, Mol. Phys. 81 (1994) 251–261, https://doi.org/10.1080/00268979400100171.
[67] F. Müller-Plathe, A simple nonequilibrium molecular dynamics method for calculating the thermal conductivity, J. Chem. Phys. 106 (1997) 6082–6085, https://doi.org/10.1063/1.473271.
[68] G. Kresse, J. Furthmüller, Efficient iterative schemes for *ab initio* total-energy calculations using a plane-wave basis set, Phys. Rev. B 54 (1996) 11169–11186, https://doi.org/10.1103/PhysRevB.54.11169.
[69] G. Kresse, D. Joubert, From ultrasoft pseudopotentials to the projector augmented-wave method, Phys. Rev. B 59 (1999) 1758–1775, https://doi.org/10.1103/PhysRevB.59.1758.
[70] J.M. Dickey, A. Paskin, Computer simulation of the lattice dynamics of solids, Phys. Rev. 188 (1969) 1407–1418, https://doi.org/10.1103/PhysRev.188.1407.
[71] Z. Fan, C. Wei, V. Vierimaa, A. Harju, Efficient molecular dynamics simulations with many-body potentials on graphics processing units, Comput. Phys. Commun. 218 (2017) 10–16, https://doi.org/10.1016/j.cpc.2017.05.003.